A&A 669, A67 (2023)
https://doi.org/10.1051/0004-6361/202244579

Astronomy & Astrophysics

Catalogue of solar-like oscillators observed by TESS in 120-s and 20-s cadence⋆

Emily Hatt[1], Martin B. Nielsen[1,2,3], William J. Chaplin[1,2], Warrick H. Ball[1,2], Guy R. Davies[1], Timothy R. Bedding[2,4], Derek L. Buzasi[5], Ashley Chontos[6], Daniel Huber[6], Cenk Kayhan[7], Yaguang Li[2,4], Timothy R. White[2,4,8], Chen Cheng[4], Travis S. Metcalfe[9], and Dennis Stello[10]

[1] School of Physics and Astronomy, University of Birmingham, Birmingham B15 2TT, UK
e-mail: exh698@student.bham.ac.uk
[2] Stellar Astrophysics Centre (SAC), Department of Physics and Astronomy, Aarhus University, Ny Munkegade 120, 8000 Aarhus C, Denmark
[3] Center for Space Science, NYUAD Institute, New York University Abu Dhabi, PO Box 129188, Abu Dhabi, United Arab Emirates
[4] Sydney Institute for Astronomy (SIfA), School of Physics, University of Sydney, Camperdown, NSW 2006, Australia
[5] Department of Chemistry and Physics, Florida Gulf Coast University, Fort Myers, FL 33965, USA
[6] Institute for Astronomy, University of Hawai'i, 2680 Woodlawn Drive, Honolulu, HI 96822, USA
[7] Department of Astronomy and Space Sciences, Science Faculty, Erciyes University, 38030 Melikgazi, Kayseri, Turkey
[8] Research School of Astronomy and Astrophysics, Mount Stromlo Observatory, The Australian National University, Canberra, Australian Capital Territory, Australia
[9] White Dwarf Research Corporation, 9020 Brumm Trail, Golden, CO 80403, USA
[10] School of Physics, University of NSW, NSW 2052, Australia

Received 21 July 2022 / Accepted 7 October 2022

ABSTRACT

Context. The Transiting Exoplanet Survey Satellite (TESS) mission has provided photometric light curves for stars across nearly the entire sky. This allows for the application of asteroseismology to a pool of potential solar-like oscillators that is unprecedented in size.
Aims. We aim to produce a catalogue of solar-like oscillators observed by TESS in the 120-s and 20-s cadence modes. The catalogue is intended to highlight stars oscillating at frequencies above the TESS 30-min cadence Nyquist frequency with the purpose of encompassing the main-sequence and subgiant evolutionary phases. We aim to provide estimates for the global asteroseismic parameters $\nu_{\rm max}$ and $\Delta\nu$.
Methods. We applied a new probabilistic detection algorithm to the 120-s and 20-s light curves of over 250 000 stars. This algorithm flags targets that show characteristic signatures of solar-like oscillations. We manually vetted the resulting list of targets to confirm the presence of solar-like oscillations. Using the probability densities computed by the algorithm, we measured the global asteroseismic parameters $\nu_{\rm max}$ and $\Delta\nu$.
Results. We produce a catalogue of 4177 solar-like oscillators, reporting $\Delta\nu$ and $\nu_{\rm max}$ for 98% of the total star count. The asteroseismic data reveal a vast coverage of the Hertzsprung-Russell diagram, populating the red giant branch, the subgiant regime, and extending towards the main sequence.
Conclusions. A crossmatch with external catalogues shows that 25 of the detected solar-like oscillators are a component of a spectroscopic binary, and 28 are confirmed planet host stars. These results provide the potential for precise, independent asteroseismic constraints on these and any additional TESS targets of interest.

Key words. asteroseismology – catalogs – stars: oscillations – methods: data analysis

1. Introduction

Asteroseismology, the study of the intrinsic oscillations of stars, has revealed the physical properties of thousands of stars to high precision (e.g. Metcalfe et al. 2014; Lebreton & Goupil 2014; Lagarde et al. 2015; Serenelli et al. 2017; Yu et al. 2018; Yıldız et al. 2019). Solar-like oscillators, wherein modes are excited and damped by the turbulent motion of gas in the outer convection zone, have been of particular interest due to the host of identifiable overtones present in their oscillation power spectra. The spectra of these stars can be characterized via two global parameters, the large frequency separation ($\Delta\nu$) and the frequency at maximum power ($\nu_{\rm max}$). The first describes the regular frequency interval separating overtone modes of a given angular degree. The second refers to the central frequency of the Gaussian-like envelope describing the visible power excess caused by the modes. These two parameters are the most readily available in the spectrum of a solar-like oscillator and, when combined with an independent measure of effective surface temperature ($T_{\rm eff}$), can be exploited to determine the mass and radius of a star to within a few percent (Silva Aguirre et al. 2012; Huber et al. 2012; Guggenberger et al. 2016; Gaulme et al. 2016; Yıldız et al. 2016; Li et al. 2021; Mathur et al. 2022).

⋆ The catalogue (full Table 2) is only available at the CDS via anonymous ftp to cdsarc.cds.unistra.fr (130.79.128.5) or via https://cdsarc.cds.unistra.fr/viz-bin/cat/J/A+A/669/A67

With the only requirement for the excitation of modes being the presence of an outer convection zone, solar-like oscillations have been observed in stars on the main sequence (e.g. Chaplin et al. 2014), in the subgiant phase (e.g. Appourchaux et al. 2012b; Mathur et al. 2022) and on the red giant branch (e.g. Bedding et al. 2010; Yu et al. 2018; Çelik Orhan et al. 2021). As a given star evolves through these phases, structural changes will affect the properties of the oscillations. The least evolved stars oscillate at a few thousand μHz. This decreases as the star evolves off the main-sequence, dropping to below ∼100 μHz on the red giant branch. Despite the large coverage of the Hertzprung-Russell (HR) diagram, current catalogues are disjoint in evolutionary state. Detections are dominated by a large number of red giants and a much smaller set of main-sequence stars, with the subgiant phase only sparsely sampled. Although a decrease in numbers is expected during this phase, given their rapid evolution, observational constraints have magnified the discrepancy.

Relying predominantly on space-based photometry means that observations of solar-like oscillators are mostly limited to data collected by a handful of missions. Of these, the *Kepler* (Borucki et al. 2010) mission provides the longest time series for a large number of available targets. Observing the same patch of sky for four years, the mission monitored approximately 196 000 targets (e.g. Huber et al. 2014). Data were collected in two modes, long and short cadence, with the associated sampling rates corresponding to Nyquist frequency limits of 283 μHz and 8496 μHz, respectively. The short cadence data span the full range in frequency where solar-like oscillations are located. However, due to telemetry constraints, the number of targets observed in the longer cadence greatly outnumbered those in short. Of the total observed targets, only a few thousand were selected for short cadence (Thompson et al. 2016). Therefore, of the tens of thousands of solar-like oscillators detected using *Kepler* data, the vast majority are more evolved stars (Stello et al. 2013; Hekker et al. 2011; Yu et al. 2018).

Although sparse in comparison, detections of solar-like oscillators were made in the short cadence data (Chaplin et al. 2011b). Due to the reduced capacity for these observations, these slots were reserved for targets most suited to the main aims of the mission: the detection of exoplanets via the transit method. This led to the preferential selection of cool main-sequence stars (Batalha et al. 2010). The combination of the selection criteria for the short cadence observations and the Nyquist frequency in the long-cadence data resulted in the asteroseismic yield lacking a significant number of subgiant stars. The largest list of these stars was constructed by Li et al. (2020) and numbers only 50 subgiants.

The TESS mission (Ricker et al. 2014) launched in 2018 and has been surveying the majority of the sky, providing an extensive database of potential solar-like oscillators. The nominal mission lasted 2 yr, and observations continue during the first extended mission, which concluded observing in September of 2022. To maximise the sky coverage, observations are made in sectors with an average length of 27.4 days. Most targets are captured in one or two sectors, while a small number of stars are located where the sectors overlap at the ecliptic poles (known as the Continuous Viewing Zones). Similarly to *Kepler*, the majority of the stars monitored by TESS in the nominal mission were observed at 30-min cadence (referred to as full-frame images, or FFIs), corresponding to a Nyquist frequency of 278 μHz. Currently, the largest systematic searches for solar-like oscillators have been performed with observations at this cadence, and they were therefore restricted to the more evolved stars (Silva Aguirre et al. 2020; Hon et al. 2021; Mackereth et al. 2021; Stello et al. 2022). Shorter cadences are available for a smaller set of targets, with the nominal mission including a 120-s integration time (double the *Kepler* short cadence). The extended mission introduced 20-s data for a reduced target list while the FFI cadence was shortened to 10 min. With Nyquist frequencies of 4167 μHz and 25 000 μHz, respectively, the 120-s and 20-s cadence data allow us to detect solar-like oscillations in less evolved solar-like oscillators.

To this end, we used 120-s and 20-s TESS data to search for oscillations in stars observed during Sectors 1 to 46. Starting with a smaller set of targets that were identified as the most likely to oscillate above the 30-min FFI Nyquist frequency (Schofield et al. 2019), we have identified 400 candidate solar-like oscillators by eye. These were used to optimise a detection algorithm presented in Nielsen et al. (2022; henceforth referred to as N22). We then passed the remaining stars observed during the aforementioned sectors to this tuned pipeline. Although the main aim of this work is to construct a list of solar-like oscillators, we found that we could exploit the probability distributions calculated by the algorithm to measure the global properties ($\nu_{\rm max}$ and $\Delta\nu$). Therefore, we provide these values for the majority of the detected solar-like oscillators.

2. Target selection

The full list of targets observed in 120-s cadence by TESS exceeds 300 000. The Asteroseismic Target List (ATL, Schofield et al. 2019) gives some indication of which stars are most likely to be solar-like oscillators prior to running the algorithm. By separating this sample from the full set of 120-s cadence targets, we can loosen detection constraints whilst keeping the required manual validation to manageable levels. To distinguish the stars in the ATL from the remaining targets observed in 120-s cadence, we refer to the latter sample as 'the Large Sample'.

The ATL was constructed prior to the launch of TESS to provide a prioritised list of targets most likely to yield detections of solar-like oscillations (Schofield et al. 2019; see also Fausnaugh et al. 2021; Godoy-Rivera et al. 2021). Aimed at 120-s cadence data, the list was restricted to stars that would oscillate above the 30-min FFI Nyquist frequency. To select targets, the authors employed asteroseismic scaling relations for $\nu_{\rm max}$ (Campante et al. 2016). This allowed them to locate stars in the TESS field of view that were predicted to have $\nu_{\rm max} > 240$ μHz. Calculating the expected power excess caused by the modes, the authors estimated the probability that the oscillations would be detectable. Only targets with a probability of at least 5% of making a detection were retained, which constituted ≈25 000 targets. Of these, 11 220 had been observed at the time of this work. In the following analysis, values of parallax and $T_{\rm eff}$ (required by the detection algorithm) were taken from the ATL. The ATL used parallaxes from *Gaia* data release 2 (GDR2; Gaia Collaboration 2018), supplemented at bright magnitudes with values from the eXtended HIPPARCOS Catalogue (XHIP; Anderson & Francis 2012). Effective temperatures in the ATL were computed from a polynomial in dereddened $(B-V)$ colour, using coefficients according to Torres (2010).

The Large Sample consists of the remaining 120-s cadence targets. We selected stars brighter than 11th magnitude in 2MASS $K_{\rm S}$ magnitude, and used $T_{\rm eff}$ from the TESS Input Catalogue (TIC; Stassun et al. 2019) to restrict to the range $4500\,{\rm K} < T_{\rm eff} < 6500\,{\rm K}$. This includes the typical ranges in $T_{\rm eff}$ of stars from the main sequence to the red giant branch, and removes stars that are likely too faint for modes to be visible

Table 1. Global asteroseismic parameters of stars in the literature sample.

Name	TIC	$\nu_{\max}$ (μHz)	$\Delta\nu$ (μHz)	Source
HD 19916	200723869	1188 ± 40	61.4 ± 1.5	TESS 120-s (1)
HD 222416	441462736	430 ± 18	28.94 ± 0.15	TESS 120-s (2)
λ^2 For	122555698	≈ 1280	69.76 ± 0.23	TESS 120-s (3)
HD 212771	12723961	226.6 ± 9.4	16.25 ± 0.19	TESS 30-min FFI (4)
HD 222076	325178933	203.0 ± 3.6	15.60 ± 0.13	TESS 120-s (5)
94 Aqr	214664574	875 ± 12	50.2 ± 0.4	TESS 120-s (6)
γ Pav	265488188	2693 ± 95	119.9 ± 1.0	TESS 20-s (7)
π Men	261136679	2599 ± 69	116.7 ± 1.1	TESS 20-s (7)
ν Ind	317019578		25.08 ± 0.10	TESS 120-s (8)
β Hyi	267211065	≈ 1000	57.24 ± 0.16	HARPS and UCLES, WIRE (9)
μ Ara	362661163	≈ 2000	89.68 ± 0.19	HARPS (10)
μ Her	460067868	1216 ± 11	64.2 ± 0.2	SONG (11)
α Men	141810080	3134 ± 440	140 ± 2	TESS 20-s (12)

References. (1) Addison et al. (2021). (2) Huber et al. (2019). (3) Nielsen et al. (2020). (4) Campante et al. (2019). (5) Jiang et al. (2020). (6) Metcalfe et al. (2020). (7) Huber et al. (2022). (8) Chaplin et al. (2020). (9) Bedding et al. (2007), Karoff et al. (2007). (10) Bouchy et al. (2005). (11) Grundahl et al. (2017). (12) Chontos et al. (2021).

(Stello et al. 2017). In this set, we analysed light curves for 255,089 stars. We applied the same cuts to all of the targets observed in 20-s cadence, which yielded light curves for 6157 stars. Parallaxes for both sets were again drawn from GDR2.

For reference, we also identified targets with a published detection of solar-like oscillations and some measure of the global asteroseismic parameters. A set of 13 such stars was produced, which is shown in Table 1 and referred to in the following as the 'literature sample'. We prioritized targets oscillating at frequencies above the *Kepler* long-cadence Nyquist as per the main aim of the catalogue. Parallaxes and effective temperatures were drawn from GDR2.

3. Data selection

We used detrended light curves produced by the TESS Science Processing Operations Center (SPOC) pipeline (Jenkins et al. 2016), which carries out the simple aperture photometry and removes instrumental trends. We used light curves recorded in 120-s cadence, except when 20-s data were available. In the literature sample, we used 120-s cadence light curves for all but three stars (γ Pav, π Men and α Men), where we used 20-s cadence light curves. We used the open source package `Lightkurve` (Lightkurve Collaboration 2018) to stitch sectors together, and remove flux values exceeding 5σ.

As TESS observes in 27.4-day sectors, there are gaps present in the light curves. During the nominal mission, the northern and southern hemispheres were each observed for 13 sectors, amounting to a total 2-yr observing run. The extended mission returned to the southern hemisphere, meaning that the light curves of some targets contain year-long gaps. Both leaving the gaps and methods to fill the gaps (e.g. linear interpolation; Stello et al. 2015) introduce strong correlations between frequency bins. Assuming mode lifetimes follow the relation given by Appourchaux et al. (2012a) (see also Lund et al. 2017), at $T_{\rm eff} = 5000$ K, we expect mode lifetimes on the order of weeks. Therefore, if a star is observed in the nominal mission and then a year later in the extended, we expect that the modes have been re-excited so that the variability in the time series is no longer correlated. Hence we removed the gap in the data by shifting the time stamps. As in N22, gaps larger than 50 days were treated in this way. Gap closing in this manner is not the optimal approach and does alter the line profiles, which would impact measurements of individual frequencies, as was discussed in Bedding & Kjeldsen (2022). However, as noted in N22, the inclusion of gaps significantly increased the false-positive rate (see N22 Fig. A.1), necessitating closing the gaps for our detection tests. Furthermore, we report only the global seismic parameters, and do not measure individual frequencies. We then used the `Lightkurve` package to produce a power density spectrum via the 'fast' Lomb-Scargle method (Lomb 1976; Scargle 1982; Press & Rybicki 1989).

4. Detection of solar-like oscillators

In the following section, we briefly review the methods used in the detection algorithm of N22 before we discuss the detections made in each set of targets. The detection test consists of two modules, which exploit different properties of solar-like oscillators:

1. Power excess test: The first module uses the power spectral density of the time series. Given the assumption that the noise in each frequency bin follows a χ^2 distribution with 2 degrees of freedom, the probability that only noise is present in a given bin is calculated (the H_0 probability). The probability that an envelope is present is then computed via a prediction of the expected power in a hypothetical envelope centred on each frequency bin (the H_1 probability). The prediction is calculated via the methods of Chaplin et al. (2011a) and Schofield et al. (2019), requiring $T_{\rm eff}$. Prior information on $\nu_{\max}$ is used, guided by parallax and 2MASS K_S-band magnitude.

2. Large separation test: The second module looks for the signature of the regularly spaced overtones. This is achieved using the methods described in Mosser & Appourchaux (2009), who used the autocorrelation function (ACF) of the time series. A band-pass filter is placed on the power spectrum at a test frequency and the ACF of this filtered time series is calculated via an inverse Fourier transform. Repeating this for other test frequencies, we produce a 2D ACF in test frequency (a proxy for $\nu_{\max}$) and lag (related to the large frequency separation via

$\tau = 1/\Delta\nu$). This 2D map is collapsed along the lag axis to produce a 1D distribution in frequency. To evaluate whether the probability the observed collapsed ACF is inconsistent with noise, N22 approximated the response due to noise by a Γ distribution.

Using 400 solar-like oscillators and non-detections manually identified from the ATL, N22 established the performance of the pipeline for a range of detection thresholds. They found that the pipeline was able to attain a true-positive rate of 94.7% and a false-positive rate of 8.2% when asking for a response in at least one of the two modules[1].

In the following sections, we discuss the detections made in the four samples via this algorithm (see Table 2). All of the reported solar-like oscillators have been manually vetted to check for false positives. We retained only targets in which are confident we have identified the presence of oscillations, prioritizing a reduced false-positive rate over maximising the yield. This may cause an under-representation of targets with a very low signal-to-noise ratio. A breakdown of the total counts, and which sample they belong to, can be seen in Table 3. Cross-referencing with NASA's Exoplanet Archive[2], we found that 28 of the stars in our catalogue are confirmed planet hosts. The majority of these stars have not yet been studied asteroseismically. Asteroseismic inferences on these targets are reserved for an upcoming work. We also cross-referenced with the Ninth Catalogue of Spectroscopic Binary Orbits of Pourbaix et al. (SB9; 2004), discovering 25 stars are components in spectroscopic binary systems.

Figure 1 shows the value of 2MASS K_S magnitude against the predicted value of ν_{max}. In grey we show targets observed in 120-s cadence with a detection probability greater than 10% using the methods described by Chaplin et al. (2011a) and Schofield et al. (2019). The gap in the grey population starting at $K_S \approx 4$ is present in the full sample of short cadence targets and is not enforced by the probability cut, which only places upper limits on ν_{max} and magnitude. This is likely the result of the TESS target selection process, which consists of selecting stars from a number of lists including cool dwarfs, known planet hosts, bright stars, hot subdwarfs, and guest investigator targets (Stassun et al. 2018, 2019). We did not detect solar-like oscillations in any targets with $\nu_{max} < 5$ μHz, regardless of magnitude. As discussed in N22, the predicted mode amplitude used in the power excess module included the observed decrease near the red edge of the δ Scuti instability strip. This was done via a factor that depends on ν_{max} and T_{eff}, so that at a given temperature, amplitudes decrease as a function of frequency (Chaplin et al. 2011a). The correction was calibrated using main-sequence stars and therefore may not be appropriate for the most evolved targets. At $T_{eff} = 4800$ K, the factor decreases to approximately zero at frequencies below 5 μHz, which suppresses detections in the power excess module. In addition, from the approximate relation between ν_{max} and $\Delta\nu$ (Stello et al. 2009, see Eq. (1)) at a ν_{max} of 5 μHz, we would expect $\Delta\nu$ to be below 1 μHz. This is approaching the resolution in a single sector of TESS data (0.4 μHz). Therefore, detections in the repeating pattern module are also increasingly unlikely.

4.1. Literature sample

Of the 13 solar-like oscillators drawn from the literature, the algorithm flagged a detection in both modules for 11 stars. μ Ara produced a response in the power excess module, but not the repeating pattern. Oscillations in this star have thus far only been detected in Doppler velocity (Bouchy et al. 2005). As the signal from granulation is lower relative to the modes in velocity measurements than in photometry (Basu & Chaplin 2017), the single-module response is likely just an effect of the decreased signal-to-noise ratio. The remaining star, HD 19916, did not produce a flag in either module. Although oscillations in HD 19916 have been detected in TESS 120-s cadence data, the authors note that a custom aperture had to be used, expanding to include more of the stellar flux (Addison et al. 2021). To maintain consistency with the rest of our catalogue, we did not mimic this approach. We note that the stars with detections reported in 20-s data (γ Pav, π Men, and α Men) produced flags in both modules. However, when we use the available 120-s data for the same stars, one is not detected at all (π Men) and the others are only detected in the power excess module, despite oscillating at frequencies well below the corresponding Nyquist frequency limit. The improvement made by the 20-s data was highlighted by Huber et al. (2022).

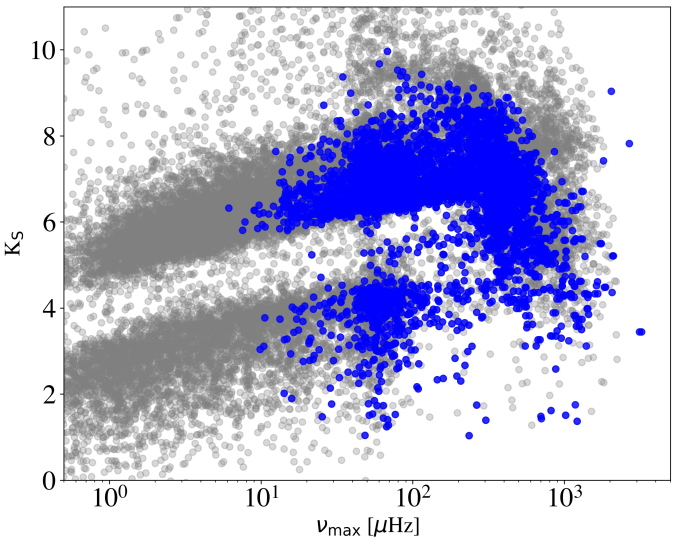

Fig. 1. 2MASS K_S magnitude and predicted ν_{max} for stars observed in 120-s cadence with a detection probability exceeding 10% (grey). The targets that we identified as solar-like oscillators are marked in blue.

4.2. Asteroseismic target list

To construct the set of stars used to establish the performance of the detection algorithm in N22, a manual inspection of the 11 220 spectra discussed in Sect. 2 was performed. On the construction of the sets of 400 oscillators and 400 'non-oscillators', several stars fell into the category of targets for which, although some excess power was present in the spectrum, we were unable to unambiguously classify the target as a solar-like oscillator. Since that work was done, new sectors of data had become available, which could facilitate unambiguous classification. We therefore reran the algorithm on the full set of 11 220 spectra. With the testing set of oscillators from N22 removed, 2651 stars were flagged in just one module and 490 in two. Of the single-module detections, the vast majority were false positives, presenting some large non-solar-type signal rather than solar-like oscillations (e.g. periodic dips caused by a transit, eclipse, or classical oscillations). These stars were not included in the

[1] This is achieved when taking a threshold of 0.77 on the power excess module and 0.73 on the frequency spacing module.
[2] https://exoplanetarchive.ipac.caltech.edu

Table 2. Seismic parameters.

TICID	No. sectors	RP	PE	$\nu_{\max}$ (μHz)	$\sigma(\nu_{\max})$ (μHz)	$\Delta\nu$ (μHz)	$\sigma(\Delta\nu)$ (μHz)	Sample	Flag
270536913	1	1	1	368.24	11.22	24.17	0.35	120-s	–
286507416	3	1	1	238.42	2.17	17.93	0.08	120-s	–
142275448	2	1	0	523.65	14.99	32.05	0.25	120-s	–
181655818	2	1	1	427.37	6.99	26.51	0.25	120-s	–
394151928	3	1	0	285.34	12.86	21.55	0.17	120-s	–
71109681	2	1	1	216.3	3.6	16.89	0.12	120-s	–
47067158	3	1	1	375.8	7.54	24.23	0.36	120-s	SB9
141201954	1	1	1	253.72	4.83	18.38	0.18	120-s	–
301558151	2	1	1	483.88	4.09	29.26	0.19	120-s	–
178199266	3	1	1	210.91	9.32	16.7	0.12	120-s	–

Notes. Catalogue of seismic parameters for detected solar-like oscillators. The full table is available at the CDS. Quantities RP and PE track which modules the target produced a detection in. Flag is 'SB9' for targets in the Ninth Catalogue of Spectroscopic Binary Orbits (Pourbaix et al. 2004) and 'PH' for targets which are confirmed planet hosts according to NASA's Exoplanet Archive.

Table 3. Detection counts in each sample.

Sample	Double	Single	Total
Literature	11	1	12
ATL	494	258	752
Large	2927	–	2927
20-s	288	198	486
Total	3720	457	4177

Notes. 'Double' refers to cases where the star flagged a detection in both the power excess and repeating pattern modules. 'Single' refers to cases where the star flagged in one module only.

metrics stated in N22. Including these stars in the false-positive metric for a single-module response increases the percentage to ≈20%. In total (with the testing set included), we detected 494 solar-like oscillators with responses in both modules, and another 258 with a single-module response.

4.3. Large sample

For the 255 089 stars for which we analysed light curves, we expect a false-positive rate of 8.2%. Assuming the majority are not solar-like oscillators, this would equate to false positives in the range of ≈20 000. We found 37 250 flagged in at least one module, therefore we took the more conservative approach and performed a manual inspection of stars that produced a flag in both modules. Of the 5781 stars that produced flags in both modules, we found 2927 clear solar-like oscillators. We have retained the list of single-module responses, but reserve releasing it until they have been manually vetted, to avoid confusion. Unlike the ATL sample, we have relaxed the requirement that $\nu_{\max}$ exceeds 240 μHz. This gives a set of targets that are cooler on average, and more strongly peaked in magnitude (see Figs. A.3 and A.2).

4.4. 20-s cadence

Of the 6157 stars in this set, the algorithm produced a single-module response for 1585, and a double-module response for 421. Upon visual inspection of these targets, we were able to clearly identify 490 solar-like oscillators.

5. Global asteroseismic parameters

Alongside enabling detection, the probability distributions calculated in the detection process allow us to measure the global asteroseismic parameters $\Delta\nu$ and $\nu_{\max}$. There are already a number of pipelines dedicated to measuring these parameters via different methods (Huber et al. 2009; Hekker et al. 2010; Kallinger et al. 2010; Mathur et al. 2010; García et al. 2014; Elsworth et al. 2017; Zinn et al. 2019). However, as the main aim of this work is the construction of a list of solar-like oscillators, a full comparison between our method and these alternatives is reserved for future work.

The probability distribution as a function of frequency calculated by the frequency spacing method (see Sect. 4) was normalized to unit integral over the spectrum, producing a probability density. The 50th percentile of this was used to measure $\nu_{\max}$, with the 16th and 84th percentiles giving the confidence interval.

N22 only required the ACF collapsed along the lag (τ) axis to perform a detection. To determine $\Delta\nu$, we instead collapsed along the test frequency. Rather than summing the ACF for all test frequencies at a given lag, we exploited the approximate relation between $\nu_{\max}$ and $\Delta\nu$ (Stello et al. 2009),

$$\frac{\tilde{\nu}_{\max}}{\nu_{\max,\odot}} = \left(\frac{\Delta\nu}{\Delta\nu_\odot}\right)^a, \tag{1}$$

where we took the value $a = 0.791$ as in N22. This estimate of $\nu_{\max}$ at a given $\Delta\nu$ ($\tilde{\nu}_{\max}$) allowed us to restrict the range of frequencies summed. Accordingly, we only summed bins in the range $|\nu_{\max} - \tilde{\nu}_{\max}| < 0.2\tilde{\nu}_{\max}$.

To calculate the expectation from a spectrum devoid of oscillations, we used 10^3 white-noise realizations. Similarly to N22, we found that for filtered white noise, the noise statistics can be well approximated by a Γ distribution in lag. The mean of this distribution can be described by the empirical relation

$$\mu(\tau) = A(B + \tau^\alpha / N_\nu^\beta), \tag{2}$$

where N_ν is the number of frequency bins included in the calculation of the ACF at a given τ. Using the `emcee` package (Foreman-Mackey et al. 2013), we fitted for the parameters B, α, and β, the results of which can be found in Table 4. Parameter A is a calibration constant that depends on the time-series length

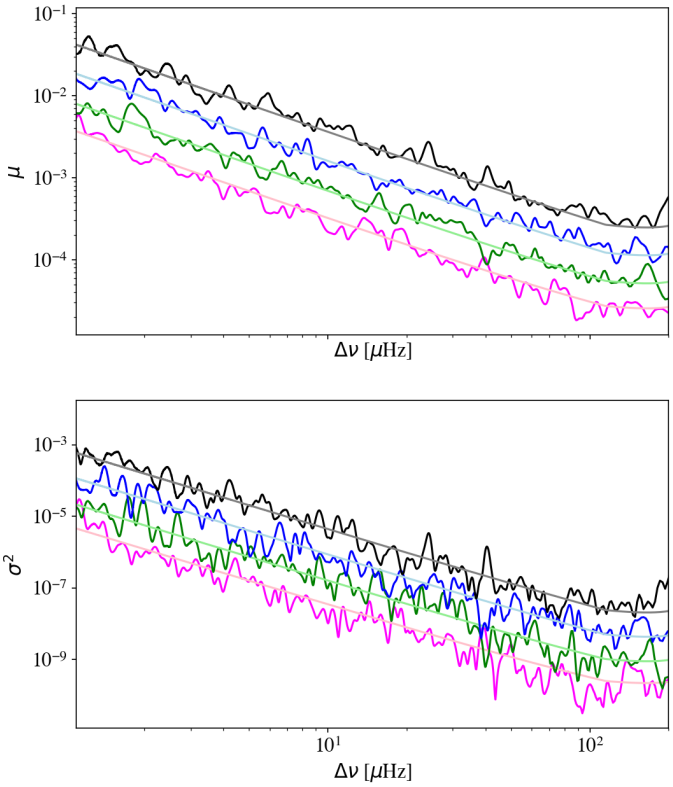

Fig. 2. Mean simulated collapsed ACF as a function of $\Delta\nu$ for filtered white noise (*top panel*). Colours represent time series of different lengths, with one sector in black, four in blue, nine in green, and twelve in magenta. Pale lines show the predictions for each length according to Eq. (2). Variance on the simulated collapsed ACF presented in the top panel (*bottom panel*).

Table 4. Parameters for Eqs. (2) and (3).

Parameter	Value
B	1.54
α	0.65
β	0.36
c	0.34

and was determined on a star-by-star basis. Using Eq. (1) to estimate the value of $\Delta\nu$ ($\widetilde{\Delta\nu}$) given the measured value of $\nu_{\rm max}$, we masked the ACF in the range $0.7\widetilde{\Delta\nu} < \Delta\nu < 1.3\widetilde{\Delta\nu}$. The calibration factor A was then estimated by the ratio of the modelled to observed ACF in the first 5 µHz and final 50 µHz (with the latter range accounting for the decrease in frequency resolution at small lag).

We found that the variance in the collapsed ACF can be approximated by

$$\sigma(\tau)^2 = c\mu(\tau)^2, \tag{3}$$

with the value of c determined by a fit to the white-noise simulations (see Table 4). A comparison of the predictions from Eqs. (2) and (3) to simulations of different time-series lengths is shown in Fig. 2. We also tested the model on data binned to different effective lengths. The net effect of the binning is an additional multiplicative factor, which is accounted for in the calibration.

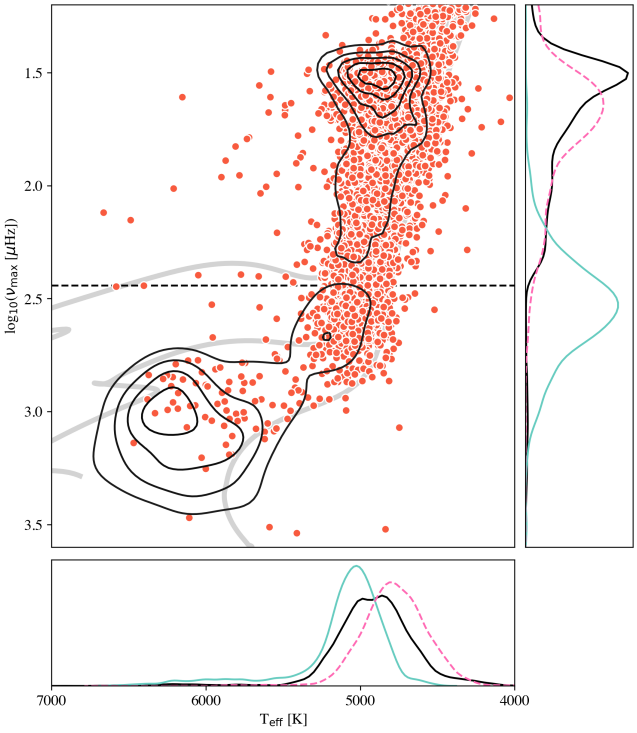

Fig. 3. Asteroseismic HR diagram for stars in all samples (*main panel*, orange circles). Effective temperatures have been drawn from the TIC in all cases, to maintain consistency. Contour lines represent measurements from *Kepler* data reported in Yu et al. (2018), Lund et al. (2017), and Serenelli et al. (2017), with effective temperatures from GDR2. The horizontal dashed line represents the *Kepler* long-cadence Nyquist frequency. Three stellar tracks at masses 1.0, 1.5, and 2.0 $M_\odot$ generated by MIST (Choi et al. 2016) are shown in grey. The distributions in $T_{\rm eff}$ and $\nu_{\rm max}$ are shown in the *bottom* and *right* panels, respectively. Here, the catalogue is split into the ATL set in turquoise and the Large Sample in pink (dashed), with the *Kepler* distribution shown in black.

We used Eqs. (2) and (3) to establish the probability ($P_{\Delta\nu}$) that the collapsed ACF (r) at a given value of τ is inconsistent with noise. Logarithmic probabilities were used for numerical stability. Given that the envelope will cause an excess above the mean, we can label any divergences below the mean as noise. Therefore, the natural choice is the survival function,

$$\log P_{\Delta\nu} = -\log\left(\int_r^\infty \frac{\beta^\alpha}{\gamma(\alpha)} r'^{,\alpha-1}\exp(-\beta r')\mathrm{d}r'\right), \tag{4}$$

where the shape parameter is $\alpha(\tau) = (\mu(\tau)/\sigma(\tau))^2$ and the scale parameter $\beta(\tau) = \mu(\tau)/\sigma(\tau)^2$. Normalizing $P_{\Delta\nu}$ to unit integral over the $\Delta\nu$ axis produces a probability density. The 50th percentile of this was used to measure $\Delta\nu$, with the 16th and 84th percentiles giving the confidence interval.

In the following sections, we discuss the values of $\Delta\nu$ and $\nu_{\rm max}$ in each of our samples. We use our Literature Sample to briefly comment on the robustness of our methods in TESS data compared to results produced largely from a bespoke analysis of individual stars. We then proceed to discuss the results in the remaining new detections. A summary of the catalogue is shown in Fig. 3. We note that in some targets, values of $\Delta\nu$ may be reported even though the star does not produce a flag in the repeating-pattern module. To report a detection, we require that the repeating-pattern merit function exceed a threshold that was chosen as the best balance between the false positives and false negatives. Therefore, a star could produce a measurable response

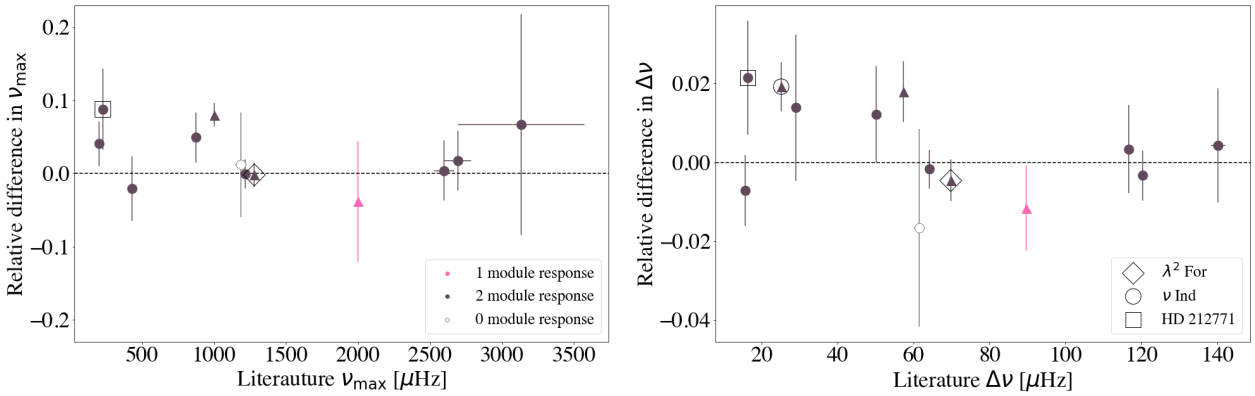

Fig. 4. Comparison of the global asteroseismic parameters measured by our algorithm to those reported in the literature. Stars are coloured by the number of modules in which they produce a flag; pink for a single module, brown for two modules, and an open grey marker for none. Triangles represent stars for which no uncertainty on ν_{max} was reported in the literature. Targets λ^2 For, ν Ind, and HD 212771, which are discussed in the text, are marked with a diamond, circle, and square, respectively. The left and right panels show the fractional difference between the values of ν_{max} and $\Delta\nu$ as measured by the algorithm vs literature value, respectively.

in the collapsed ACF, while the merit function peaks just below the selected threshold. Accordingly, we only removed measurements from the final catalogue that were manually identified as clear outliers in the ν_{max}-$\Delta\nu$ plane. The values that have been removed are shown in Fig. A.1.

5.1. Literature sample

Of the 13 targets making up the sample, 9 have published ν_{max} values with uncertainties. In the remaining stars, the authors focussed on determining individual frequencies rather than global parameters, and so estimates of ν_{max} without uncertainties were published. A comparison of the literature values to those measured by our method is shown in Fig. 4. On average, the measured values of ν_{max} are higher than those reported in the literature by ≈2.5%. The star with largest fractional difference is HD 212771, where our value of ν_{max} is higher by ≈9%. The literature value was measured using FFI data processed by the TESS Asteroseismic Science Operations Center (TASOC) pipeline (Handberg et al. 2021). From visual inspection of the signal-to-noise ratio spectrum of HD 212717, we found that the envelope extended beyond the FFI Nyquist frequency. The attenuation caused by the sampling integration causes a decrease in power near the Nyquist frequency, which could have caused an underestimate on ν_{max} in Silva Aguirre et al. (2020). Visual inspection of the power spectra confirms that our higher value is more accurate.

In total, 11 stars have measurements of $\Delta\nu$ in the literature. In the case of ν Ind, the most recent asteroseismic study was made in Chaplin et al. (2020), where the authors used a single sector of TESS data to fit individual modes. We measured $\Delta\nu$ from the gradient of a linear fit to the radial mode frequencies as a function of order (White et al. 2011). We took the same approach for λ^2 For, where similarly the authors did not provide estimates of $\Delta\nu$ (Nielsen et al. 2020). A comparison of the values with those from the algorithm is shown in the right panel of Fig. 4. The agreement is better than for ν_{max}, with a mean fractional difference on $\Delta\nu$ of 0.24%.

5.2. Asteroseismic target list

Of the 752 validated solar-like oscillators, we report both $\Delta\nu$ and ν_{max} for 739. In the majority of cases, the determination is linked: both come from the autocorrelation function collapsed along the relevant axis. However, it is possible to detect the envelope without a signal from the frequency spacing.

In order to assess the quality of the measured ν_{max} and $\Delta\nu$ values, we exploited the approximate scaling relation between the two (Eq. (1)). Although there is a slight mass dependence in exponent a (Stello et al. 2009), the general trend remains such that stars disagreeing significantly with the rest of the population may indicate an error in one (or both) of the measured values.

Figure 5 shows the relation between the values of ν_{max} and $\Delta\nu$ for the targets in the ATL sample. The majority of the stars with detections in both modules follow Eq. (1). The star with smallest $\Delta\nu$ is TIC 381975502 (CD-56 1110). Here, a background eclipsing binary introduced several harmonic peaks in the power spectral density at low frequency. These peaks appear in the ACF as a large response at a test frequency corresponding to the frequency of the orbital harmonics, resulting in the algorithm incorrectly assigning both $\Delta\nu$ and ν_{max}. This is also the case for TIC 271701447 (HR 4749; HD 108570). The values of ν_{max} and $\Delta\nu$ for these targets have been removed from the final catalogue, while IDs have been retained.

For targets detected in just one module, there is a larger scatter about the scaling relation, as shown on Fig. 5. Using an exponent on Eq. (1) of $a = 0.791$ as calculated in N22, $\Delta\nu$ for 13 targets differs by more than 30% from the value predicted by the scaling relation and measured value of ν_{max}. We performed a manual inspection of these stars and found that four are likely misclassifications. A further two passed the detection threshold, both at the envelope and at a much lower frequency, biasing the resulting parameters. In three stars, the estimated ν_{max} used in the prior was significantly higher than the observed value. They are overestimated by factors of three, five, and two. In these cases, the parallaxes reported in the ATL were drawn from XHIP rather than GDR2. The ν_{max} predicted using GDR2 parallaxes produced a prior more consistent with the measured ν_{max}. The remaining stars could be divided into two sets: Targets with less than one full sector of data, and high-ν_{max} targets with low-mode amplitudes. The resulting low signal-to-noise ratio could impact the determination of $\Delta\nu$. Values of ν_{max} and $\Delta\nu$ for these outliers have been removed.

In Fig. 3, the stars in the ATL sample cluster about the base of the red giant branch and extend toward the main sequence. The peak of the distribution falls just above the *Kepler* long-cadence

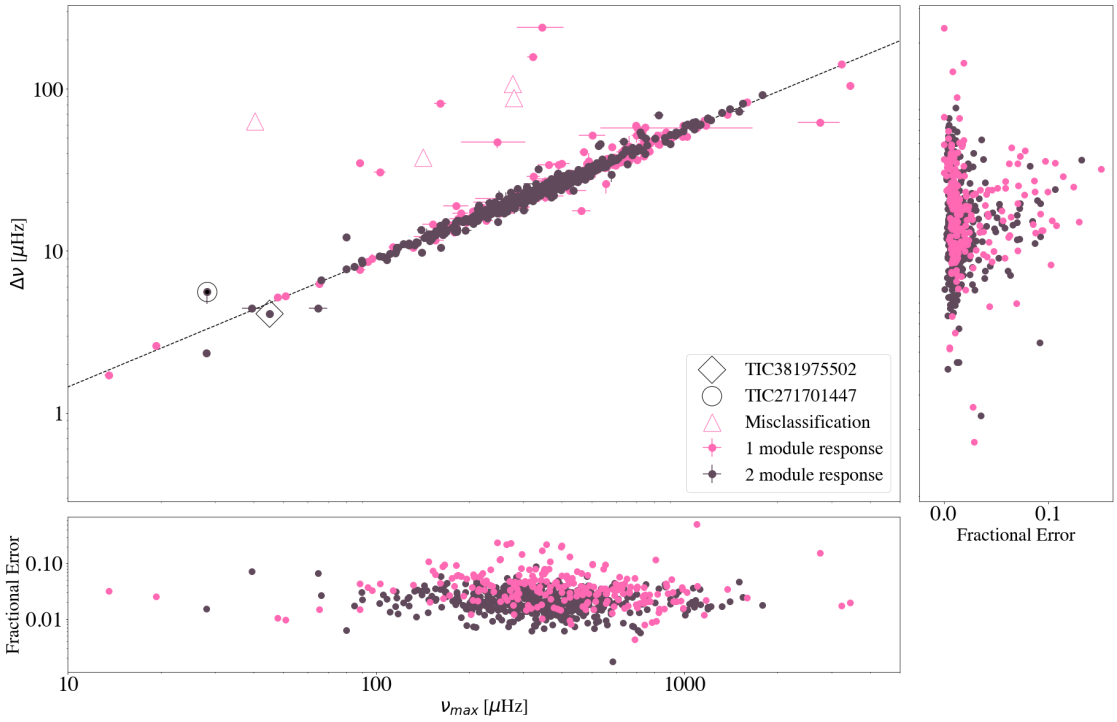

Fig. 5. $\Delta\nu$ as a function of $\nu_{\rm max}$ measured by the algorithm for validated solar-like oscillators from the ATL set (*main panel*). Stars producing flags in only one module are shown in pink, and those producing flags in both modules are shown in brown. Triangles mark stars that were likely misclassified as solar-like oscillators. Targets TIC381975502 and TIC271701447, which are discussed in the text, have been marked with a diamond and circle. The dotted black line shows Eq. (1). *Additional panels* show the fractional uncertainties on $\Delta\nu$ and $\nu_{\rm max}$.

Nyquist frequency, populating the previously sparsely sampled region. The density falls off toward higher $\nu_{\rm max}$, which is likely a result of the decreasing mode amplitude.

5.3. Large sample

Here, we report both $\nu_{\rm max}$ and $\Delta\nu$ for all but 62 stars. For these outliers, we found similar issues to those discussed in the ATL. Additionally, we noted 16 stars for which the probability distributions in $\nu_{\rm max}$ were multi-modal. The remaining targets vastly outnumber those from the ATL, and span the red giant branch (as shown in Fig. 3). The density increases with decreasing $\nu_{\rm max}$ until it peaks at ≈49 μHz. At the high-$\nu_{\rm max}$ tail, we note an overlap between the ATL and Large Sample. There are 119 stars that did not appear in the ATL even though they show oscillations at frequencies above 240 μHz. Of these, just under half lie near the ATL cutoff, with $240 < \nu_{\rm max} < 300$ μHz. A total of 63 stars, however, are above 300 μHz in a region that should be included in the ATL. There are several reasons why these targets could have been omitted. The estimate of $\nu_{\rm max}$ in the ATL was a function of $T_{\rm eff}$, such that a significant underestimate on the latter could have pushed the former beyond the enforced 240 μHz cut. Calculating $T_{\rm eff}$ for the additional targets using the methods stated in the ATL, we did not find a systematic underestimate compared to GDR2, with values agreeing to within 10% in over 90% of the targets. The other possibility is that the detection probabilities for these targets were underestimated. This could be the result of an overestimated noise level caused by, for example, an underestimation of the size of the predicted pixel mask or a greater degree of contamination from background sources. A full comparison between the predictions in the ATL and the observed yield is reserved for future work.

According to the main aim of the TESS mission (Ricker et al. 2014), we expected that targets proposed for 120-s cadence would be less evolved than the giants presented here. Although targets were also selected when they were brighter than $T_{\rm mag} = 6$ (where $T_{\rm mag}$ is the magnitude of the star for the TESS instrument response), which would preferentially select bright giants, we found that ≈80% of the giants in which we detected solar-like oscillations were fainter than this limiting magnitude. We therefore checked that the oscillations occur in the star associated with the TIC number being searched, rather than in another star in the mask, by comparing the $\nu_{\rm max}$ value predicted by the prior to the detected value (see Fig. 6). In general, the ratio of the two was close to unity, indicating that the detected envelope belongs to the target in question.

5.4. 20-s cadence

The measured values of $\Delta\nu$ and $\nu_{\rm max}$ are shown in Fig. 7. A total of 16 stars were removed by manual identification. We note that the uncertainties on $\Delta\nu$ presented in Fig. 7 appear larger than those presented in Fig. 5 (the ATL sample), which is likely due to the population of targets at $\nu_{\rm max} < 100$ μHz. The mean fractional uncertainty on the measured $\Delta\nu$ in the 20-s-cadence sample is 2.1%, approximately consistent with 1.9% in the ATL sample. Again, we find that the population is dominated by evolved stars, with the distribution peaking at a $\nu_{\rm max}$ value of 50 μHz.

We note a detection in an oscillator observed by *Kepler* (KIC 6106415; HD 177153; 'Perky'), which is a clear outlier in Fig. 7. The algorithm reports a $\Delta\nu$ of 131 μHz despite reporting a $\nu_{\rm max}$ of 127 μHz. Using *Kepler* data, oscillations were identified at $\nu_{\rm max} = 2249$ μHz (Lund et al. 2017). The envelope we detected at 127 μHz (which can be visually identified) appears

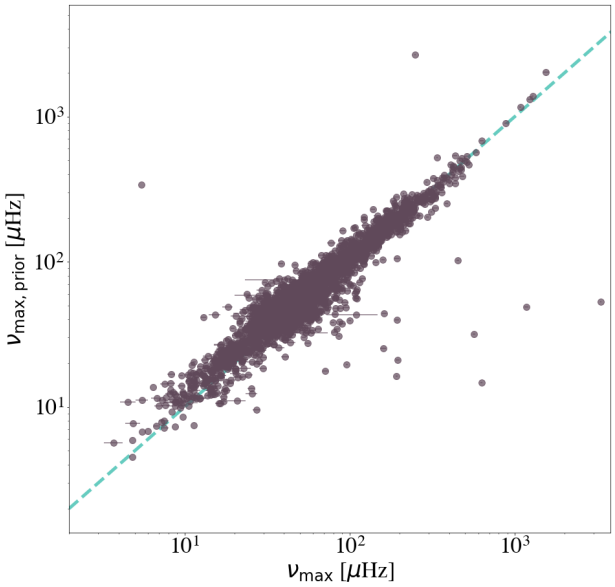

Fig. 6. Prior $\nu_{\rm max}$ ($\nu_{\rm max,prior}$) vs. measured values in short cadence targets. The dashed blue line represents the 1–1 line.

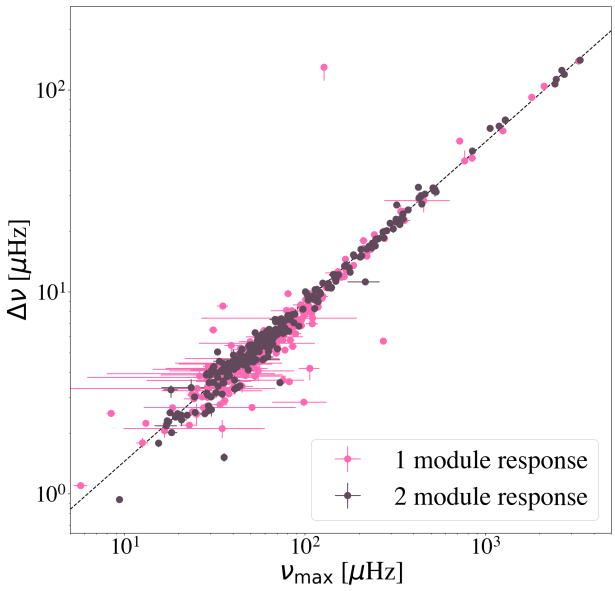

Fig. 7. $\Delta\nu$ vs. $\nu_{\rm max}$ for validated solar-like oscillators from the 20-s cadence set. Stars producing flags in only one module are shown in pink, and those producing flags in both are in plotted in brown.

to be on another red giant in the pixel mask. Therefore, the prior has caused an erroneous measurement of $\Delta\nu$.

6. Conclusions

Applying the algorithm introduced by Nielsen et al. (2022) to 120-s- and 20-s-cadence observations from the TESS mission spanning Sectors 1 to 46, we have detected solar-like oscillations in a total of 4177 targets. Of these, 12 belong to a set of previously reported solar-like oscillators, 752 to stars that appeared in the ATL, and 486 were detected using 20-s-cadence data. The remaining are targets brighter than 11th magnitude in 2MASS $K_{\rm S}$, with temperatures in the range 4500 K < $T_{\rm eff}$ < 6500 K, observed in 120-s cadence. Since Sector 46, data for additional

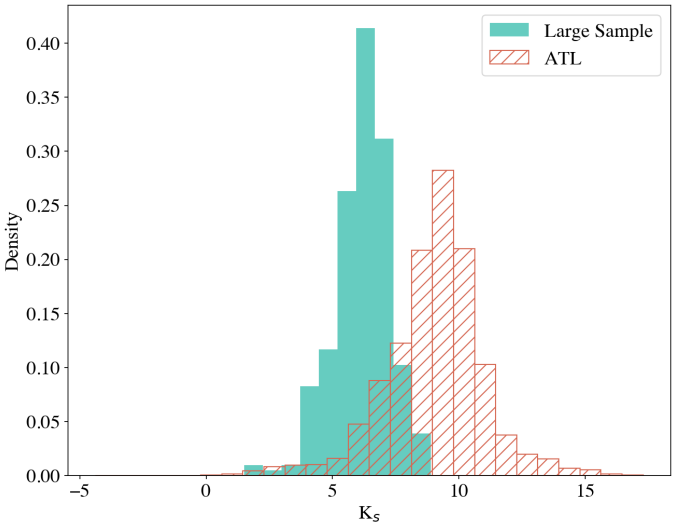

Fig. 8. Distribution in $K_{\rm S}$-band magnitude for the detections from the large sample that have values of $\nu_{\rm max}$ > 240 μHz, and those made from targets included in the ATL.

sectors have been released. We leave the analysis of these and the data collected in upcoming sectors as we approach the end of the first extended mission for future work.

All catalogued targets have been manually vetted to confirm the presence of oscillations. We note that signals from eclipsing binaries, classical pulsators, or transiting planetary bodies can cause false-positive detections. Therefore, we highlight that when using the algorithm presented in N22 with very large data sets, the more conservative approach (asking for responses in both modules) is the most effective at reducing the amount of manual vetting required.

We have extended the work of N22 to include methods for measuring the global asteroseismic parameters, $\nu_{\rm max}$ and $\Delta\nu$. We introduced a new model for parameterizing the collapsed ACF to produce a probability density for $\Delta\nu$. Applying this technique to the catalogue of detections, we measured the global asteroseismic parameters for 98% of the targets. Overlaying these stars on the asteroseismic HR diagram ($\nu_{\rm max}$ and $T_{\rm eff}$) allowed us to confirm the ATL successfully identified the least evolved stars, with little overlap in the remaining detections. The small set of stars that appear to have been missed by the ATL cluster about $K_{\rm S}$ = 6 mag (see Fig. 8), which is a region where the GDR2 astrometric solutions are known to have inferior astrometry (Lindegren et al. 2018), suggesting an issue in the parallaxes.

This catalogue demonstrates the significant contribution that the TESS mission can make to the field of asteroseismology. When targets from the ATL are isolated, the increase in the number of detections between the 280 μHz cutoff enforced by the 30-min FFI observations and the upper edge of our catalogue at around 1000 μHz is at least twofold on the detections made in *Kepler* data. With the inclusion of the stars detected in 120-s cadence that did not appear in the ATL, we were able to use a homogeneous data set to measure asteroseismic values in solar-like oscillators from the subgiant regime through the red giant branch.

Acknowledgements. Funding for the TESS mission is provided by the NASA's Science Mission Directorate. E.J.H., W.J.B. and G.R.D. acknowledge the support of Science and Technology Facilities Council. T.R.B. acknowledges support from the Australian Research Council (Discovery Project DP210103119). M.B.N.

acknowledges support from the UK Space Agency. C.K. is supported by Erciyes University Scientific Research Projects Coordination Unit under grant number DOSAP MAP-2020-9749. D.B. acknowledges support from NASA through the Living With A Star Program (NNX16AB76G) and from the TESS GI Program under awards 80NSSC18K1585 and 80NSSC19K0385. D.H. acknowledges support from the Alfred P. Sloan Foundation and the National Aeronautics and Space Administration (80NSSC21K0652). T.S.M. acknowledges support from NASA grant 80NSSC22K0475. The authors acknowledge use of the Blue-BEAR HPC service at the University of Birmingham. This paper includes data collected by the *Kepler* mission and obtained from the MAST data archive at the Space Telescope Science Institute (STScI). Funding for the Kepler mission is provided by the NASA Science Mission Directorate. This work has made use of data from the European Space Agency (ESA) mission *Gaia* (https://www.cosmos.esa.int/web/gaia), processed by the *Gaia* Data Processing and Analysis Consortium (DPAC, https://www.cosmos.esa.int/web/gaia/dpac/consortium). Funding for the DPAC has been provided by national institutions, in particular the institutions participating in the *Gaia* Multilateral Agreement. This publication makes use of data products from the Two Micron All Sky Survey, which is a joint project of the University of Massachusetts and the Infrared Processing and Analysis Center/California Institute of Technology, funded by the National Aeronautics and Space Administration and the National Science Foundation.

References

Addison, B. C., Wright, D. J., Nicholson, B. A., et al. 2021, MNRAS, 502, 3704
Anderson, E., & Francis, C. 2012, Astron. Lett., 38, 331
Appourchaux, T., Benomar, O., Gruberbauer, M., et al. 2012a, A&A, 537, A134
Appourchaux, T., Chaplin, W. J., García, R. A., et al. 2012b, A&A, 543, A54
Basu, S., & Chaplin, W. 2017, Asteroseismic Data Analysis: Foundations and Techniques, eds. S. Basu, & W. J. Chaplin, Princeton Series in Modern Observational Astronomy
Batalha, N. M., Borucki, W. J., Koch, D. G., et al. 2010, ApJ, 713, L109
Bedding, T. R., & Kjeldsen, H. 2022, RNAAS, 6, 179
Bedding, T. R., Kjeldsen, H., Arentoft, T., et al. 2007, ApJ, 663, 1315
Bedding, T. R., Huber, D., Stello, D., et al. 2010, ApJ, 713, L176
Borucki, W. J., Koch, D., Basri, G., et al. 2010, Science, 327, 977
Bouchy, F., Bazot, M., Santos, N. C., Vauclair, S., & Sosnowska, D. 2005, A&A, 440, 609
Campante, T. L., Schofield, M., Kuszlewicz, J. S., et al. 2016, ApJ, 830, 138
Campante, T. L., Corsaro, E., Lund, M. N., et al. 2019, ApJ, 885, 31
Çelik Orhan, Z., Yıldız, M., & Kayhan, C. 2021, MNRAS, 503, 4529
Chaplin, W. J., Kjeldsen, H., Bedding, T. R., et al. 2011a, ApJ, 732, 54
Chaplin, W. J., Kjeldsen, H., Christensen-Dalsgaard, J., et al. 2011b, Science, 332, 213
Chaplin, W. J., Basu, S., Huber, D., et al. 2014, ApJS, 210, 1
Chaplin, W. J., Serenelli, A. M., Miglio, A., et al. 2020, Nat. Astron., 4, 382
Choi, J., Dotter, A., Conroy, C., et al. 2016, ApJ, 823, 102
Chontos, A., Huber, D., Berger, T. A., et al. 2021, ApJ, 922, 229
Elsworth, Y., Hekker, S., Basu, S., & Davies, G. R. 2017, MNRAS, 466, 3344
Fausnaugh, M., Morgan, E., Vanderspek, R., et al. 2021, PASP, 133, 095002
Foreman-Mackey, D., Hogg, D. W., Lang, D., & Goodman, J. 2013, PASP, 125, 306
Gaia Collaboration (Brown, A. G. A., et al.) 2018, A&A, 616, A1
García, R. A., Mathur, S., Pires, S., et al. 2014, A&A, 568, A10
Gaulme, P., McKeever, J., Jackiewicz, J., et al. 2016, ApJ, 832, 121
Godoy-Rivera, D., Tayar, J., Pinsonneault, M. H., et al. 2021, ApJ, 915, 19
Grundahl, F., Fredslund Andersen, M., Christensen-Dalsgaard, J., et al. 2017, ApJ, 836, 142
Guggenberger, E., Hekker, S., Basu, S., & Bellinger, E. 2016, MNRAS, 460, 4277
Handberg, R., Lund, M. N., White, T. R., et al. 2021, AJ, 162, 170
Hekker, S., Broomhall, A. M., Chaplin, W. J., et al. 2010, MNRAS, 402, 2049
Hekker, S., Elsworth, Y., De Ridder, J., et al. 2011, A&A, 525, A131
Hon, M., Huber, D., Kuszlewicz, J. S., et al. 2021, A 'Quick Look' at All-Sky Galactic Archeology with TESS: 158,000 Oscillating Red Giants from the MIT Quick-Look Pipeline
Huber, D., Stello, D., Bedding, T. R., et al. 2009, Commun. Asteroseismol., 160, 74
Huber, D., Ireland, M. J., Bedding, T. R., et al. 2012, ApJ, 760, 32
Huber, D., Silva Aguirre, V., Matthews, J. M., et al. 2014, ApJS, 211, 2
Huber, D., Chaplin, W. J., Chontos, A., et al. 2019, AJ, 157, 245
Huber, D., White, T. R., Metcalfe, T. S., et al. 2022, AJ, 163, 79
Jenkins, J. M., Twicken, J. D., McCauliff, S., et al. 2016, SPIE Conf. Ser., 9913, 99133E
Jiang, C., Bedding, T. R., Stassun, K. G., et al. 2020, ApJ, 896, 65
Kallinger, T., Mosser, B., Hekker, S., et al. 2010, A&A, 522, A1
Karoff, C., Bruntt, H., Kjeldsen, H., Bedding, T., & Buzasi, D. L. 2007, Commun. Asteroseismol., 150, 147
Lagarde, N., Miglio, A., Eggenberger, P., et al. 2015, A&A, 580, A141
Lebreton, Y., & Goupil, M. J. 2014, A&A, 569, A21
Li, Y., Bedding, T. R., Li, T., et al. 2020, MNRAS, 495, 2363
Li, Y., Bedding, T. R., Stello, D., et al. 2021, MNRAS, 501, 3162
Lightkurve Collaboration (Cardoso, J. V. d. M., et al.) 2018, Lightkurve: Kepler and TESS time series analysis in Python, Astrophysics Source Code Library
Lindegren, L., Hernández, J., Bombrun, A., et al. 2018, A&A, 616, A2
Lomb, N. R. 1976, Ap&SS, 39, 447
Lund, M. N., Silva Aguirre, V., Davies, G. R., et al. 2017, ApJ, 835, 172
Mackereth, J. T., Miglio, A., Elsworth, Y., et al. 2021, MNRAS, 502, 1947
Mathur, S., García, R. A., Régulo, C., et al. 2010, A&A, 511, A46
Mathur, S., García, R. A., Breton, S., et al. 2022, A&A, 657, A31
Metcalfe, T. S., Creevey, O. L., Doğan, G., et al. 2014, ApJS, 214, 27
Metcalfe, T. S., van Saders, J. L., Basu, S., et al. 2020, ApJ, 900, 154
Mosser, B., & Appourchaux, T. 2009, A&A, 508, 877
Nielsen, M. B., Ball, W. H., Standing, M. R., et al. 2020, A&A, 641, A25
Nielsen, M. B., Hatt, E., Chaplin, W. J., Ball, W. H., & Davies, G. R. 2022, A&A, 663, A51
Pourbaix, D., Tokovinin, A. A., Batten, A. H., et al. 2004, A&A, 424, 727
Press, W. H., & Rybicki, G. B. 1989, ApJ, 338, 277
Ricker, G. R., Winn, J. N., Vanderspek, R., et al. 2014, SPIE Conf. Ser., 9143, 914320
Scargle, J. D. 1982, ApJ, 263, 835
Schofield, M., Chaplin, W. J., Huber, D., et al. 2019, ApJS, 241, 12
Serenelli, A., Johnson, J., Huber, D., et al. 2017, ApJS, 233, 23
Silva Aguirre, V., Casagrande, L., Basu, S., et al. 2012, ApJ, 757, 99
Silva Aguirre, V., Stello, D., Stokholm, A., et al. 2020, ApJ, 889, L34
Stassun, K. G., Oelkers, R. J., Pepper, J., et al. 2018, AJ, 156, 102
Stassun, K. G., Oelkers, R. J., Paegert, M., et al. 2019, AJ, 158, 138
Stello, D., Chaplin, W. J., Basu, S., Elsworth, Y., & Bedding, T. R. 2009, MNRAS, 400, L80
Stello, D., Huber, D., Bedding, T. R., et al. 2013, ApJ, 765, L41
Stello, D., Huber, D., Sharma, S., et al. 2015, ApJ, 809, L3
Stello, D., Zinn, J., Elsworth, Y., et al. 2017, ApJ, 835, 83
Stello, D., Saunders, N., Grunblatt, S., et al. 2022, MNRAS, 512, 1677
Thompson, S. E., Fraquelli, D., Van Cleve, J. E., & Caldwell, D. A. 2016, Kepler Archive Manual, Kepler Science Document KDMC-10008-006
Torres, G. 2010, AJ, 140, 1158
White, T. R., Bedding, T. R., Stello, D., et al. 2011, ApJ, 743, 161
Yıldız, M., Çelik Orhan, Z., & Kayhan, C. 2016, MNRAS, 462, 1577
Yıldız, M., Çelik Orhan, Z., & Kayhan, C. 2019, MNRAS, 489, 1753
Yu, J., Huber, D., Bedding, T. R., et al. 2018, ApJS, 236, 42
Zinn, J. C., Stello, D., Huber, D., & Sharma, S. 2019, ApJ, 884, 107

Appendix A: Additional plots

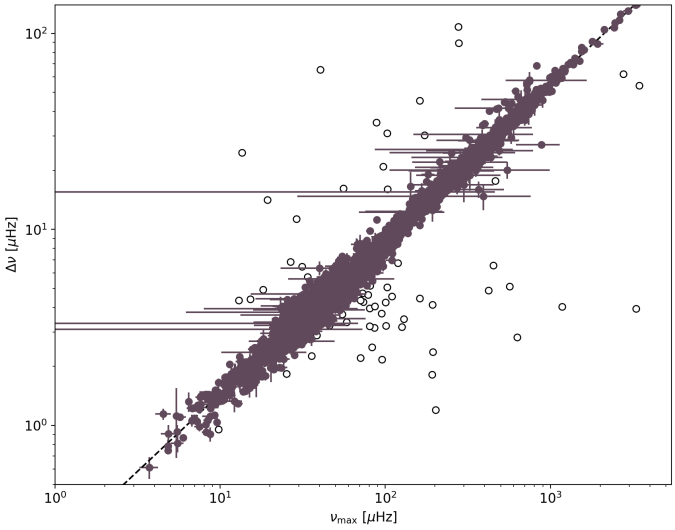

Fig. A.1: $\Delta\nu$ as a function of ν_{max} for targets in the final catalogue in brown. Values that were removed after manual identification are shown as open circles.

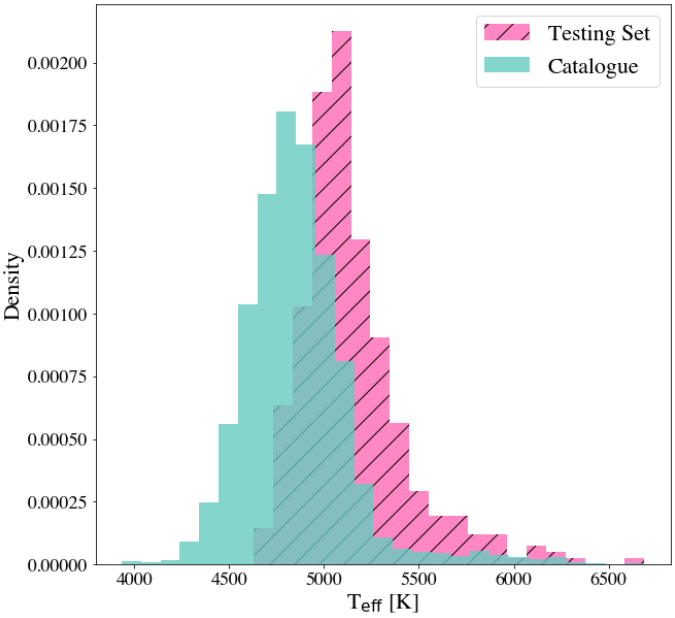

Fig. A.2: Distribution of T_{eff} for targets used in the testing set of 400 oscillators from N22 compared to those in the catalogue reported here.

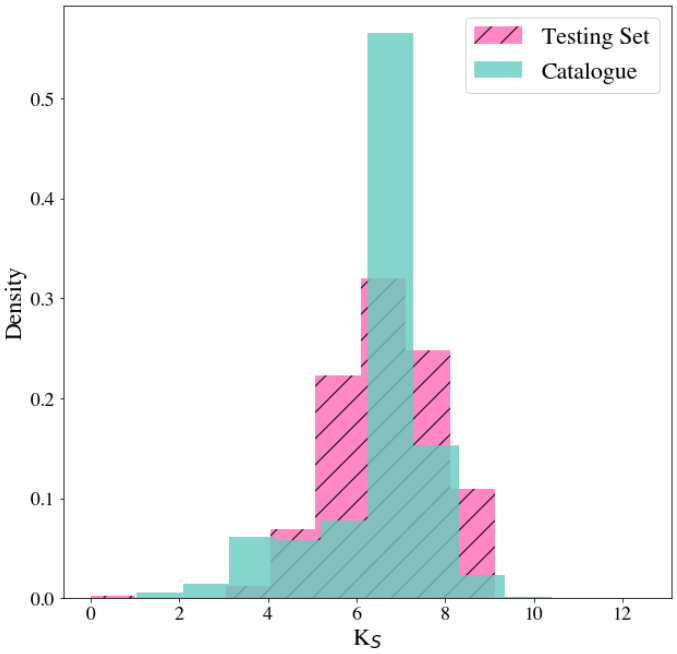

Fig. A.3: As in figure A.2 with 2MASS K_S magnitude.